nature communications

Article

https://doi.org/10.1038/s41467-026-71146-z

Direct observations of atmospheric oxidized mercury speciation in polar areas

Received: 7 July 2025

Accepted: 6 March 2026

Published online: 07 April 2026

Check for updates

Tuija Jokinen[1,2] ✉, Juan Carlos Gómez Martín[3], Aryeh Feinberg[4], Anoop S. Mahajan[5], John M. C. Plane[6], A. Ulises Acuña[4], Carlos Cuevas[4], Juan Z. Dávalos[4], Lauriane L. J. Quéléver[2], Tiia Laurila[2], Ivo Beck[7], Julia Schmale[7], Heikki Junninen[8], Mikko Sipilä[2], Markku Kulmala[2], Tuukka Petäjä[2] & Alfonso Saiz-Lopez[4] ✉

Mercury is a persistent pollutant with significant public health impacts in polar regions where fish consumption drives human exposure. Atmospheric oxidation pathways control where mercury deposits globally, but the lack of molecular-level observations of oxidized mercury products has hindered the validation of proposed chemical mechanisms. Here, we show the in-situ online detection of individual mercuric halides ($HgCl_2$, BrHgCl, $HgBr_2$, ClHgI, BrHgI, and HgI_2) in the polar boundary layer using atmospheric pressure chemical ionization mass spectrometry. Our observations identify $HgBr_2$ as the dominant oxidized mercury species at both poles, while $HgCl_2$ and other halides were also observed in Antarctica. The observed speciation diverges from current model predictions, which favor $HgCl_2$ and HOHgBr as dominant oxidized forms. Our results show that real-time molecular measurements can substantially advance global mercury monitoring and improve the chemical models used to assess environmental policies and predict deposition patterns.

Understanding mercury speciation in the atmosphere is crucial for identifying the lifecycle of mercury contamination in the environment. Atmospheric elemental mercury (Hg^0) is relatively inert and insoluble, allowing it to persist (lifetime of 6–20 months) and be transported globally[1,2]. Hg^0 oxidation by halogen and hydroxyl radicals[3,4] converts it to soluble gaseous oxidized mercury (Hg^{II}, collectively known as GOM) that is rapidly washed out by precipitation[3,5]. GOM drives roughly half of all atmospheric mercury deposition[5], with models estimating that up to 80% of Hg^{II} deposition occurs over the ocean[2,6]. Once deposited, Hg^0 methylates in aquatic systems to form neurotoxic methyl mercury that further bioaccumulates in fish and wildlife[7]. Polar regions are hotspots for this cycle, especially during spring when photochemical activation of saline snowpack releases reactive bromine, triggering ozone-depletion events and rapid Br radical oxidation of Hg^0 to Hg^{II} within hours[8]. This intense halogen chemistry leads to seasonal GOM deposition pulses, which, upon incorporation into marine food webs, threatens Arctic communities dependent on seafood[8–11]. However, an ongoing uncertainty in polar Hg budgets, as well as an understanding of global Hg cycling in general, is the lack of methods to directly measure the molecular speciation of oxidized mercury.

The balance between atmospheric Hg^0 and Hg^{II} is driven by complex redox chemistry that remains highly uncertain[4,12]. This hinders our understanding of the major reaction pathways of atmospheric Hg and predicting Hg inputs to ecosystems. Much of the current knowledge about this chemistry derives from quantum chemical calculations[4,12] and chemical-transport models[3]. Despite chemical-transport models now tracking 20–30 GOM tracers[3,13], their predictions rest on theoretical rate constants and pre-concentrated denuder

[1]Climate and Atmosphere Research Center (CARE-C), The Cyprus Institute, Nicosia, Cyprus. [2]Institute for Atmospheric and Earth System Research (INAR)/Physics, University of Helsinki, Helsinki, Finland. [3]Instituto de Astrofísica de Andalucía-Consejo Superior de Investigaciones Científicas (CSIC), Granada, Spain. [4]Department of Atmospheric Chemistry and Climate, Institute of Physical Chemistry Blas Cabrera, CSIC, Madrid, Spain. [5]Indian Institute of Tropical Meteorology, Ministry of Earth Sciences, Pune, India. [6]School of Chemistry, University of Leeds, Leeds, UK. [7]Extreme Environments Research Laboratory, École Polytechnique Fédérale de Lausanne, Sion, Switzerland. [8]Institute of Physics, University of Tartu, Tartu, Estonia. ✉e-mail: t.jokinen@cyi.ac.cy; a.saiz@csic.es

data that are subject to various biases[14]. Laboratory kinetic experiments, as well as direct, real-time molecular field measurements, have remained mostly out of reach due to the extremely low ambient concentrations (pg m^{-3}) and toxicity of Hg[15,16], leaving key reaction pathways unvalidated. Conventional GOM measurement methods rely on hours-to-days of pre-concentration on KCl denuders[17] or cation-exchange/nylon membranes[14,16,18–21] followed by offline analysis, which limits molecular detail and time resolution and hinders direct molecular-level validation.

In this work, we present direct in-situ observations of several mercuric halides in the polar regions, using the nitrate-based Chemical Ionization–Atmospheric Pressure interface–Time of Flight (CI-APi-TOF) mass spectrometry technique together with ambient anion composition measurements (APi-TOF)[22,23]. In Antarctica, measurements ran over the 2014–2015 austral summer at the Finnish research station Aboa (73°03′ S, 13°25′ W)[24]. In the central Arctic, the data from the spring leg (April–June 2020, > 80° N) of the MOSAiC expedition were analyzed alongside collocated O_3, BrO, and Hg^0 observations[25,26]. Further details are provided in the methods section. Our observations reveal unexpected GOM speciation that challenges existing models of Hg redox chemistry and provides critical data to refine global mercury deposition patterns.

Results

Molecular identification of mercuric halides

Using the CI-APi-TOF, we directly detected neutral mercuric halides in ambient air at both polar sites, confirming each species by exact mass-to-charge ratios and natural abundance isotope patterns (Table S1). In Antarctica, six mercuric halides were identified: $HgCl_2$, BrHgCl, $HgBr_2$, ClHgI, BrHgI, and HgI_2 (Fig. 1), all observed exclusively as NO_3^- clusters (e.g. as $HgBr_2{\cdot}NO_3^-$). In the central Arctic, $HgBr_2$ was the only detected neutral species in April (Fig. 2), and by June the signal was below limit of detection (LOD, Fig. S1). Other GOM species were either below the LOD or masked by local ship-emitted interferences (cf. "Methods"). In Antarctica, we also observed naturally charged ions corresponding to $HgCl_2NO_3^-$, $BrHgClNO_3^-$, and $HgBr_2NO_3^-$ (Fig. S2). In the central Arctic, these naturally charged species were not detected, likely due to low concentrations and a different inlet configuration that increased losses (cf. Methods). These naturally charged ions are likely formed by ambient NO_3^- ions clustering with mercuric halides (Fig. S3). Similar experimental evidence of ambient nitrate ion clustering has been observed with highly oxygenated molecules (HOM) and sulfuric acid[27]. The concurrent detection of neutral and naturally charged ions provides a robust validation of our findings of mercuric halides in the ambient atmosphere.

We use theoretical calculations to further support the detection of neutral mercuric halide clustering with NO_3^- (cf. "Methods" for details). Ab initio calculations of the XHgY + NO_3^- ↔ XHgY· NO_3^- equilibria (X,Y = OH, Cl, Br, I) under typical inlet conditions (1 bar, residence time $\tau_{res} \approx 300$ ms, $[NO_3^-] \approx 10^7$ cm^{-3}) yield equilibrium ratios >1 and slow dissociation (Table 1) when assuming near kinetic limit charging of XHgY species with NO_3^- ($k = 10^{-10}$ cm^3 $molecule^{-1}$ s^{-1}). This suggests selective clustering of pure mercuric halides and a lack of sensitivity towards species such as $Hg(OH)_2$ or HOHgBr[3]. The absence of these signals in the CI-APi-TOF reflects the selectivity of the chemical ion-chemistry employed, rather than the true absence of these compounds in ambient air. However, the observations are consistent with the APi-TOF measurements, where neither anion nor cation measurements in Antarctica showed any indication of $Hg(OH)_2$ or HOHgBr ion cluster signals in ambient air, which suggests either the absence of the compounds at our measurement location or inefficient charging of these compounds to form ions.

Abundance and comparison with conventional methods

We quantified the mercuric halide concentrations by utilizing the gas-phase, kinetic limit calibration used with gaseous H_2SO_4[28], which ionizes with NO_3^- mainly by proton transfer. This approach has been applied previously to quantify HIO_3[29], chlorine oxyacids[30] and highly

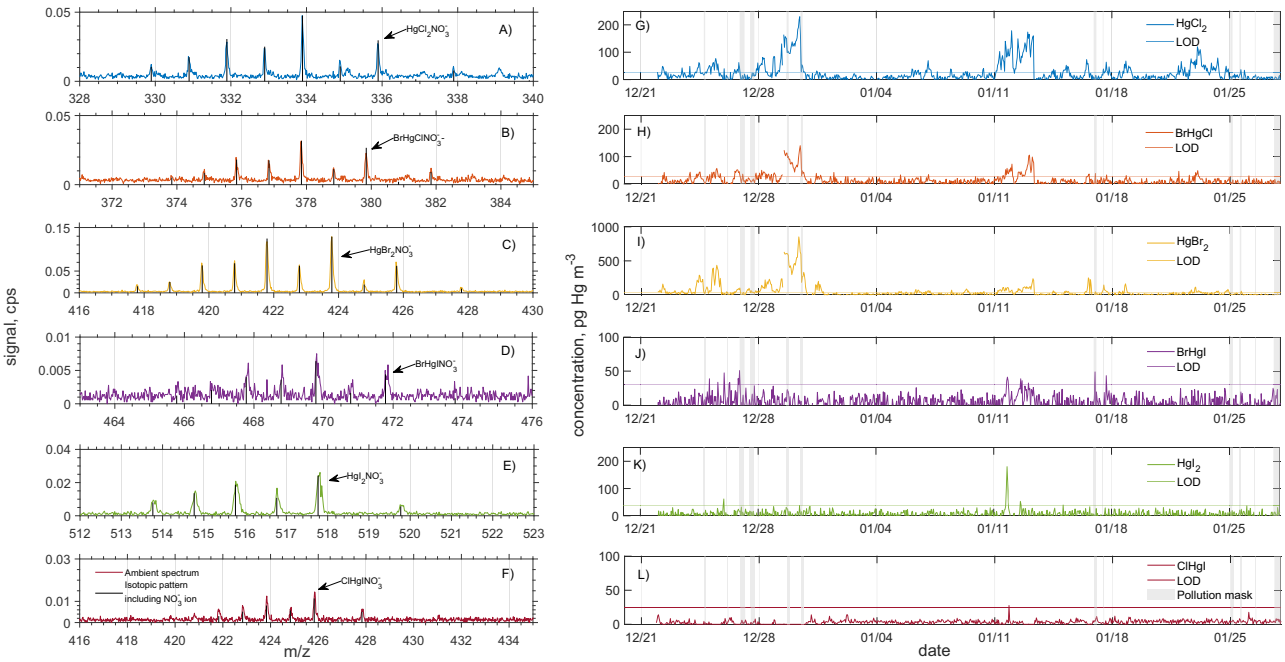

Fig. 1 | Antarctic ambient-air mass spectra and time series of mercuric halides. **a**–**f** Hourly-averaged example spectra of neutral mercuric halides charged by nitrate ions. $HgCl_2{\cdot}NO_3^-$, $BrHgCl{\cdot}NO_3^-$ and $HgBr_2{\cdot}NO_3^-$ spectra were measured on 29 November 2014, and $BrHgI{\cdot}NO_3^-$, $HgI_2{\cdot}NO_3^-$ and $ClHgI{\cdot}NO_3^-$ on 11 January 2015 at Aboa, Antarctica. Black vertical bars show theoretical isotopic patterns, while integrated peak areas were used to derive concentrations. The most abundant isotopic composition is depicted with arrows. **g**–**l** One-hour time series of the corresponding mercuric halide concentrations. Dashed lines mark the limit of detection (LOD, 3σ + baseline signal; Table S2 and "Methods"), and grey shaded regions indicate periods when the wind originated from the polluted sector (210°–270°).

https://doi.org/10.1038/s41467-026-71146-z

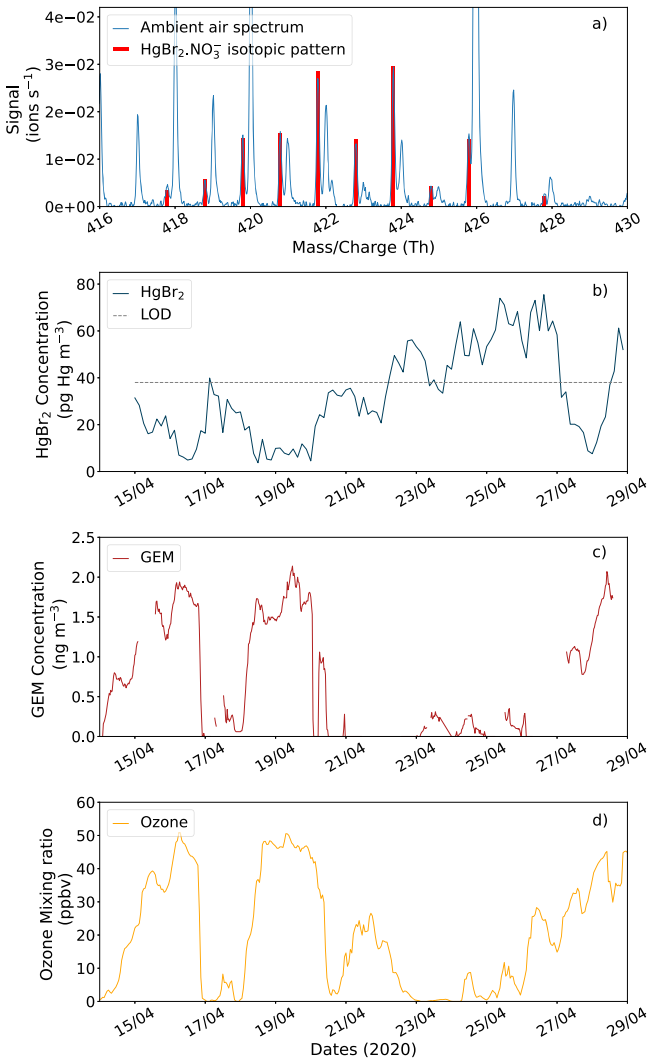

Fig. 2 | Central Arctic ambient air spectrum and time series of trace species. **a** Mass spectrum of $HgBr_2{\cdot}NO_3^-$ recorded on 25 April 2020, with the theoretical isotope pattern (red bars), **b** $HgBr_2$ concentration time series during the MOSAiC campaign in the spring (15–29 April 2020). The dashed line depicts the limit of detection (LOD). CI-APi-TOF data in (**a**) and (**b**) are averaged over 180 min to improve signal-to-noise ratio, **c** Collocated gaseous elemental mercury (GEM, Hg^0) measurements, and (**d**) Collocated ozone (O_3) measurements.

Table 1 | Thermodynamic quantities and kinetics for $XHgY.NO_3^-$ cluster ions (X,Y = OH, Cl, Br, I) at 298 K calculated at the B3LYP/aug-cc-pVQZ level of theory

Cluster ion	$\Delta_r H°$ /kJ mol^{-1}	$\Delta_r G°$ /kJ mol^{-1}	K_{eq} /cm^3 molecule^{-1}	k_{diss} /s^{-1}	Equilibrium ratio [XHgY.NO$_3^-$]/[XHgY]
$HOHgBr.NO_3^-$	−93.9	−54.1	1.2×10^{-10}	0.81	1.2×10^{-3}
$Hg(OH)_2.NO_3^-$	−84.7	−44.1	2.2×10^{-12}	44.8	2.2×10^{-5}
$HgCl_2.NO_3^-$	−107.7	−73.6	3.2×10^{-7}	3.1×10^{-4}	3.2
$BrHgCl.NO_3^-$	−108.0	−72.3	1.9×10^{-7}	5.2×10^{-4}	1.9
$HgBr_2.NO_3^-$	−108.3	−74.63	5.0×10^{-7}	2.0×10^{-4}	5.0
$BrHgI.NO_3^-$	−107.0	−71.4	1.3×10^{-7}	7.6×10^{-4}	1.3
$HgI_2.NO_3^-$	−105.9	−72.0	1.7×10^{-7}	5.8×10^{-4}	1.8

The reaction enthalpy and Gibbs energy changes are indicated respectively by $\Delta_r H°$ and $\Delta_r G°$. The equilibrium constants (K_{eq}) between XHgY + NO_3^- and $XHgY{\cdot}NO_3^-$ were obtained from ab initio calculations of $\Delta_r G°$. These were further used to calculate cluster dissociation rates k_{diss} and equilibrium ratios for typical CI-inlet working conditions (p = 1 bar, residence time = 300 ms, [NO_3^-] = 10^7 ions cm^{-3}), assuming near kinetic limit charging of XHgY species with NO_3^- ($k = 10^{-10}$ cm^3 s^{-1} molecule^{-1}) Geometries of clusters can be obtained from SI.

oxygenated organic molecule concentrations[31]. Ab initio calculations of the XHgY + NO_3^- ↔ $XHgY{\cdot}NO_3^-$ equilibria yield large binding enthalpies (Table 1) and cluster lifetimes $\tau_{diss} \gg \tau_{res}$ (~300 ms). However, the equilibrium ratios [$XHgY{\cdot}NO_3^-$]/[XHgY] ($\approx$1–5) are not »1, implying lower ionization efficiencies. Thus, the concentrations reported here should be viewed as lower limits.

Time series of Antarctic mercuric halides (Fig. 1, right column) are reported in pg Hg m^{-3} at standard temperature and pressure (STP) to facilitate comparison with prior GOM studies. Mercuric halides are abundant and chemically diverse in Antarctica, exhibiting periods when $HgBr_2$ and $HgCl_2$ peak at several hundred pg Hg m^{-3}. On January 11, three mercuric iodide species were identified: HgI_2, BrHgI, and ClHgI. All compounds show values above the LOD, which is estimated between 25 and 37 pg Hg m^{-3} for 60 min time resolution (Table S2 and "Methods" for LOD determination). Note that the LOD is determined using three times the standard deviation of the measured baseline during the whole campaign; this baseline changed with environmental conditions such as temperature inside the measurement cabin. Thus, the given LOD values should be taken as conservative values. In Antarctica, the abundance of $HgBr_2$ is potentially controlled by the presence of atmospheric bromine (Fig. S4), as evidenced by the moderate to strong correlation (r = 0.72) between the $HgBr_2$ signal and the Br^- signal (78.9189 Th, Thomson, likely from HBr[30]).

In the central Arctic (Fig. 2), $HgBr_2$ reached ~80 pg Hg m^{-3} during April but fell below the LOD by June (Fig. S5). Other halides, neutral or naturally charged, were undetected or spectrally unresolved throughout the observation period. Although ship emissions introduced an abundance of interfering peaks, CI-APi-TOF measurements of H_2SO_4, CH_3SO_3H, HIO_3 were mostly unaffected, indicating negligible effect on the mass spectrometric measurements[32]. Hence, we can infer that stack emissions during MOSAiC and pollution from the Aboa station are not the source of GOM (Figs. 1, S5). Collocated Hg^0 data[33–35] reveal that $HgBr_2$ maxima coincide with Hg^0 depletion events, mirroring ozone variability and underscoring the tight coupling of mercury speciation to bromine photochemistry[35–37].

The total concentration of mercuric halides in Antarctica (interquartile range, IQR, 29–110 pg Hg m^{-3}, full range: <LOD – 1177 pg Hg m^{-3}) lies well within the 5–705 pg Hg m^{-3} range reported across Antarctica by pre-concentration methods that lumped together all Hg^{II} compounds[38] (Fig. 3). In the central Arctic, springtime $HgBr_2$ concentrations during MOSAiC (IQR 17–49 pg Hg m^{-3}) mirror reactive gaseous mercury Tekran measurements at the Canadian Alert station in April 2020 (IQR 29–70 pg Hg m^{-3}) and at the Svalbard Zeppelin station in April 2019 (IQR 6–24 pg Hg m^{-3})[39,40]. Because Tekran measurements have been suggested to underestimate total GOM concentration[14], we also compared our data to reactive mercury (GOM + particulate Hg) values from cation-exchange membrane detection at Zeppelin (IQR 37–86 pg Hg m^{-3})[40,41]. We note, however, that the reactive mercury measurements also include also a contribution from particulate Hg[39], which would not be measured by CI-APi-TOF.

Comparison with model simulations

The close agreement across methods indicates that $HgBr_2$ constitutes a major fraction of spring GOM in the polar regions, contradicting current atmospheric models and our understanding of Hg redox chemistry. GEOS-Chem, a Hg chemical-transport model, predicts that oxidized mercury is dominated globally by $HgCl_2$ (49%), followed by particulate Hg (22%), $Hg(OH)_2$ (19%), and HOHgBr (9%)[3], reflecting oxidation via the Br, OH, and Cl pathways, which all involve second-step oxidation by O_3[3,4,15]. The WACCM chemistry-climate model also reports $HgCl_2$ to be the dominant atmospheric oxidized mercury

https://doi.org/10.1038/s41467-026-71146-z

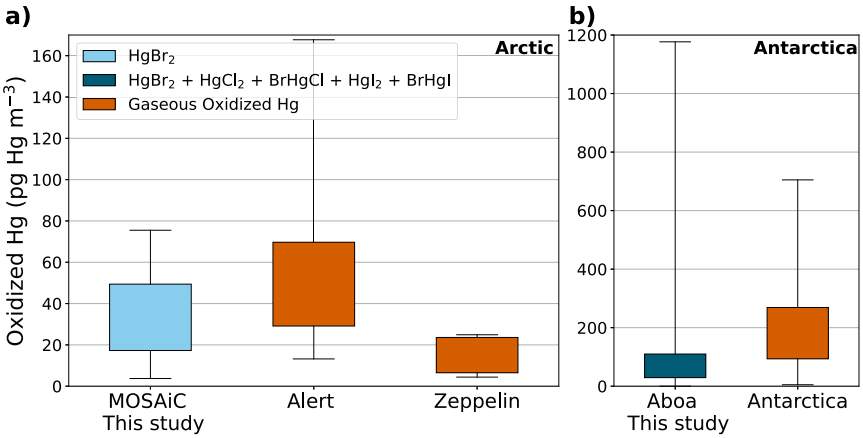

Fig. 3 | Comparison of CI-APi-ToF measurements with gaseous oxidized mercury (GOM) observations from other studies. a Box-and-whisker plots (interquartile range, IQR, min–max) of GOM in the central Arctic and Antarctica. MOSAiC CI-APi-TOF measurements from this study are from April 2020. Alert Tekran GOM measurements were from the Environment and Climate Change Canada network for April 2020. Zeppelin (Svalbard, Norway) April 2019 measurements of GOM from a Tekran instrument from Osterwalder et al.[40] **b** Tekran GOM measurements for Antarctic sites were reviewed in the literature by Dommergue et al.[38] and spanning all seasons.

species, with a minor contribution (< 0.1%) of $HgBr_2$ globally[42]. Photochemical model simulations of the polar springtime period predict that $HgCl_2$ and HOHgBr are the major components of GOM, with other Hg^{II} species contributing minor amounts (< 0.3%) (Fig. S6). Compared to these modeling estimates, the CI-APi-TOF observations reveal that a much broader range of Hg^{II} species contribute to the total observed GOM mass concentration in the polar regions. In the central Arctic spring, $HgBr_2$ was the only GOM species detected above the LOD, accounting for essentially all of the CI-APi-TOF–measured GOM mass (Fig. 2), directly contradicting model predictions. In fact, the only point of agreement between existing models and our measurements in Antarctica is the presence of $HgCl_2$ as an important oxidized Hg species. Because CI-APi-TOF does not detect HOHgBr or $Hg(OH)_2$, their true ambient levels remain unknown, but the agreement and similarity of the measured mercuric halide concentrations to previous GOM measurements suggest that the species detected here are major contributors to the GOM mass. Therefore, the discrepancy between modelled and detected species points strongly to missing reaction channels in current chemistry schemes, including the role of iodine in oxidizing mercury.

These discrepancies have profound implications for deposition estimates. Each Hg^{II} species exhibits unique photolysis rates, particle uptake efficiencies, and solubilities[12,13,43,44]. These are the properties that govern atmospheric lifetime and hence transport distance. For example, $HgBr_2$ photolyzes roughly three orders of magnitude faster than $HgCl_2$[45]. Thus, if $HgBr_2$ is a more dominant GOM species than $HgCl_2$, as our measurements suggest, this would enhance the photoreduction of GOM and reformation of Hg^0, increasing the possibility of long-range transport of Hg. Refining the Hg chemistry schemes in chemical transport models to better represent measured Hg^{II} speciation could lead to strong shifts in regional deposition patterns, with direct consequences for ecosystem exposure assessments.

Discussion

The direct molecular identification of gas-phase mercuric halides in polar field campaigns with CI-APi-TOF constitutes a major step forward in unravelling atmospheric mercury recycling. By revealing the unexpected dominance of pure halides, particularly $HgBr_2$, and the presence of mercuric iodides (HgI_2, BrHgI, ClHgI)[46], our observations expose critical gaps in current redox-chemistry schemes and underscore the need to revisit the mechanisms that govern Hg^0 oxidation. Further analysis of these new speciation insights is required to identify the missing chemical reactions that can be incorporated into chemical transport models. The inclusion of these missing pathways will improve predictions of regional mercury deposition and help clarify how photolysis, heterogeneous reactions, and halogen availability drive the polar mercury cycle.

Reanalysis of archived CI-APi-TOF datasets from earlier ground-based[47], shipborne[48], and airborne[49] campaigns could further illuminate GOM speciation trends across seasons and environments. Going forward, targeted calibration of individual mercuric halide responses and strategic deployments of CI-APi-TOF instruments will extend real-time molecular speciation into urban, marine, and free-tropospheric settings. Such comprehensive speciation data will deepen our understanding of oxidation pathways and Hg recycling on a global scale, ultimately guiding more accurate assessments of ecosystem exposure and informing mitigation efforts under frameworks like the Minamata Convention on mercury.

Methods

Sampling location in Antarctica

This study conducted observations during two campaigns in polar regions. In Antarctica, measurements took place at the Finnish research station Aboa (73°03′S, 13°25′W), in Queen Maud Land, located ~130 km inland from the coast at 480 meters above sea level. Spanning the austral summer months with midnight sun conditions, the campaign lasted from November 2014 to February 2015. The aerosol laboratory utilized in the campaign was situated ~200 m upwind from the main station and any pollution sources[24]. Polluted periods when the wind was blowing from the main station (wind direction 210-270°)[50] were occasionally observed, but do not have any significant effect on the measurements (Fig. 1). Data availability extends over the whole austral summer, but only a period after 21 December was considered in this study due to a suspected leak in the mass spectrometric system prior to this date. For all other campaign measurements (meteorological parameters, aerosol number concentrations, and aerosol precursor concentrations) refer to Jokinen et al.[24].

Sampling location in the Arctic

In the central Arctic, observations were conducted as part of the ship-based Multidisciplinary Drifting Observatory for the Study of Arctic Climate (MOSAiC) campaign on R/V Polarstern[25]. The CI-APi-TOF was located in the bow of the ship in the "Swiss container" and the APi-TOF in the container behind the Swiss container. This Arctic campaign unfolded from October 2019 to the end of September 2020 in the central Arctic region[25]. We selected a springtime period (April 2020)

for further investigation due to the event known as a "bromine explosion" in the springtime Arctic atmosphere. In addition, we selected another period in late spring-early summer (June 2020) to understand the relevance of oxidants (ozone, bromine) to our observations. The location of the ship during the spring leg 3 can be visualized from Fig. 2 in Shupe et al[25]. The disadvantage of executing measurements on a drifting vessel is that the pollution from the ship's exhaust can be pushed towards the sampling location with the wind. The wind direction was often unfavorable for measuring pollution-free air masses during spring. Due to this, we used a pollution mask that was developed for detecting particle pollution from the ship's stack[51]. The effects of the pollution in our measurements, particularly on the identification of peaks in the mass spectra, is discussed below.

Chemical ionization−atmospheric pressure interface−time-of-flight mass spectrometer (CI-APi-TOF)

In both campaigns, a nitrate-based CI-APi-TOF mass spectrometer (Tofwerk, Switzerland, "HTOF", with finite resolving power of approximately m/Δm ≈ 4000–4500) with a so-called "Eisele" type CI-inlet was employed[23]. In short, the CI-APi-TOF consists of three core parts: the chemical ionization inlet, atmospheric pressure interface, and the time-of-flight analyzer. In the CI-inlet, charger ions are produced by exposing concentrated nitric acid (HNO_3, 3–5 mlpm) contained in a sheath flow (20–30 lpm) to a soft X-ray source. The total flow of the system was 30–40 lpm in order to achieve the best isokinetic flow dynamics. The difference between the total and sheath flow is equal to the sample flow of approximately 10 lpm, which was checked weekly. The two flows inside the CI-inlet are coaxial to eliminate any interaction with the walls. The drift time (reaction time) between the sample and charger ions is ~300 ms, which prevents ion-induced nucleation occurring inside the inlet. Sample ionization in the CI system occurs at ambient pressure for better sensitivity than low pressure systems. The charger ions (NO_3^-, $(HNO_3)_{1\text{-}2}NO_3^-$) produced are pushed into the sample flow using an electric field (ion source -125 V, drift tube −100 V). Sample charging happens through proton transfer between nitrate ions (or its multimers) and the sample molecule or via clustering of the sample compound (e.g in the case of $HgBr_2$ or oxygenated organic molecules) with the charger ion. All reported mercury-containing compounds in this study were detected with a NO_3^- ion (e.g. as $HgBr_2NO_3^-$).

In Aboa, the sample was drawn in via an unheated ~60 cm ¾" polished stainless-steel tube. In the MOSAiC campaign, we used an insulated but unheated "New Particle Formation" NPF-inlet that was specifically designed to minimize diffusional losses with high inlet total flow of about 70 lpm. The NPF-inlet was ~1.3 m long, with a diameter of 10.2 cm, connected to the ¾" inlet tube of the CI-inlet with a flange. Even when operated at extreme conditions in polar regions, the inlets do not frost due to high flow rates and no salt depositions were observed. The residence time of the sample air in the sampling line is approximately 1 s (60 cm tube with 10 lpm flow), which is likely too fast to cause any significant wall effects on the ambient samples.

Atmospheric pressure interface time of flight mass spectrometer (APi-TOF)

The APi-TOF consists of an Atmospheric Pressure interface (APi) that allows sampling from ambient air directly to the time-of-flight (TOF) mass spectrometer[22]. The TOF analyser is identical with the CI-APi-TOF (Tofwerk, Switzerland, "HTOF", with finite resolving power of approximately m/Δm ≈ 4000–4500). The sampling flow to the instrument is ~0.8 lpm through a 0.3 mm diameter pinhole. The ambient air sample is drawn to the pinhole at 10–20 lpm using a vacuum pump. The inlet in Aboa was a polished stainless-steel tube, 10 mm in diameter, with a 10 lpm flow rate and approximately 1 m in length. In MOSAiC, we had to opt for a vertical inlet line, again made of 10 mm stainless-steel, through the roof of the container. This inlet was ~2 m in length with a core sampling style inlet sampling at 20 lpm to decrease diffusional losses. The length of the inlet might have caused some decrease in the ion signal.

In Aboa and MOSAiC, most of the campaign was sampled using negative polarity settings to sample anions. This is to target observations of mostly acidic and highly oxygenated organic compounds and molecular clusters, connected to new particle formation events. In Aboa, we sampled two days of cations in positive polarity between 26 and 29 January and a week during MOSAiC at the end of July.

The observations represent the naturally charged molecules and clusters produced mainly by cosmic radiation. The decay of radon also produces ions, but the concentration is extremely low over the ocean and in Antarctica. Ion collisions with neutral molecules will transfer the charge in energetically favourable situations. In the case of anions, the most abundant signals in daytime are bisulfate, iodate and their clusters, and nitrate ions during nighttime. In positive polarity, strong bases such as pyridines dominate the spectra[22].

Quantification of mercuric halides

The data analysis for this study was conducted using tofTools software version 613 built on Matlab[22]. The analysis employed an average time of 180 min for MOSAiC data and 60 min for Aboa data. The original data time resolution was 5 s. Both CI-APi-TOF data sets were baseline corrected. Mass calibration was performed utilizing the known compounds in the spectra. The Aboa spectra were mass calibrated using the 2-parameter model with 3 most favorable options from NO_3^-, $HNO_3NO_3^-$, $(HNO_3)_2NO_3^-$, $(HNO_3)_3NO_3^-$, $HgCl_2NO_3^-$ and $HgBr_2NO_3^-$. The mean mass accuracy was 5.3 ppm and always <15 ppm. MOSAiC spectra were mass calibrated using the same 2-parameter model and 3 most favorable options from NO_2^-, $NO_2[^{18}O]^-$, $HNO_3NO_2[^{18}O]^-$, $(HNO_3)_2NO_2[^{18}O]^-$, $C_3F_5O_2^-$. The mean mass accuracy was 2.9 ppm and always <5 ppm.

The concentration of mercuric halides was calculated as:

$$[mercuric\ halide]_{neutral} = \frac{Mercuric\ halide{\cdot}NO_3^-\ peak\ area}{\sum Reagent\ ion\ peak\ area} xC \quad (1)$$

where $[\text{mercuric halide}]_{\text{neutral}}$ is the calculated concentration (in molecules/cm^3) of the neutral measured mercuric halide, mercuric halide·NO_3^- peak area is the measured signal including all detected isotopic peaks as integrated peak area. The reagent ion peak areas are the sum of the observed nitrate signals (fitted peak areas): NO_3^-, $HNO_3NO_3^-$ and $(HNO_3)_2NO_3^-$. C is a calibration factor. C was obtained from a sulfuric acid calibration in molecules cm^{-3} which is commonly used in aerosol precursor observations. For Aboa, $C = 1.195 \times 10^{10}$ molecule cm^{-3} and MOSAiC $C = 6 \times 10^9$ molecule cm^{-3}. Both calibrations were done using the original inlet tubing, so the calibration factor includes all diffusional losses.

The conversion from molecule cm^{-3} to mass concentration (pg Hg m^{-3}) was calculated using a constant factor of 3.333×10^{-4} ($= 200.59\ g\ mol^{-1} / 6.02 \times 10^{23}\ molecule\ mol^{-1} \times 10^{12}\ pg\ g^{-1} \times 10^6\ cm^3\ m^{-3}$) to better compare with previous total GOM measurements.

Detection limit for mercuric halides

The sensitivity of the CI-APi-TOF instrument is relatively high with low detection limits, only obscured by the baseline signal due to the constant feed of charger ion-containing gas into the system, and electronic noise. In our processing workflow (tofTools), background correction is always applied before further analysis. The limit of detection (LOD) of the instruments used at Aboa (60 min time resolution, observations in January 2015) and the MOSAiC (180 min time resolution, observations in April 2020) campaign are given in Table S2.

For the present study, the limit of detection (LOD) was determined separately for the Aboa and MOSAiC datasets because the

baseline characteristics and the presence of interfering peaks significantly differed between the sites (Fig. S8).

Aboa: At Aboa, a 24 h period at the end of the campaign, between 26 and 27 Jan 2015, showed no detectable peaks at the m/z values of any mercury-halide species. The LOD was calculated by adding three times the standard deviation of the unit mass resolution signal (so called signal integration region, SIR, 0.4 Th width) on the average baseline deducted signal during this clean interval. This provided a stable and physically meaningful baseline (LOD), independent of short-term variability in temperature or counting statistics.

MOSAiC: At the MOSAiC site, the mercury-halide m/z values always contained contributions from overlapping organic ions (double or partially resolved peaks, Fig. S8). Consequently, a clean baseline interval comparable to Aboa did not exist. Instead, we estimated the noise from the inter-peak signal, i.e., the local minima between transient organic peaks. This region corresponds to the Noise Integration Region (NIR) in tofTools.

Because the NIR represents the lowest ion counts within the same Δm/z extraction window used for quantifying the analyte (the Signal Integration Region, SIR), it provides the most accurate and internally consistent estimate of the noise when neighboring peaks are present. The NIR can include low-level contributions from unresolved ions, which results in slightly higher LODs compared to a clean SIR baseline; however, this approach is standard for TOF mass spectrometers and necessary for masses where true zero-signal periods do not exist. LODs for MOSAiC were computed as 3σ of this NIR signal for each m/z.

Estimating bromine content

We use the CI-APi-TOF and the APi-TOF to provide proxies for atmospheric bromine content. In the CI-APi-TOF, Br^- signal is a trace of e.g. neutral HBr. It could also originate from the Br^- fragment from other bromine-containing molecules that charge with the aforementioned charger ions. The identification of Br^- is based on both the exact mass and isotopic pattern. The peak areas normalized by charger ions (CI-APi-TOF) and anion signal (APi-TOF) reported in Fig. S3 (Aboa) corresponds to Br^- (78.9189 Th). For the Br- signal recorded during MOSAiC, refer to Tham et al[30].

Polluted periods

In the case of MOSAiC, the mass spectra were occasionally heavily polluted with exhaust from the ship's stack. Pollution created abundant signals on the same m/z unit masses as the studied mercuric halides, and thus we may not always separate the mercuric halide peaks (e.g. $HgCl_2$ or BrHgCl) from overlapping and dominant peaks at the same mass. In order to separate nearby peaks with similar masses, one should have mass resolving power owning instruments. Better resolution instrumentation should to be used for mercuric halide analysis in the future.

Ab initio quantum calculations

Calculations were performed with the Gaussian 16 suite of programs[52], using the hybrid density functional/Hartree−Fock B3LYP method together with Dunning's quadruple-ζ aug-cc-pVQZ correlation consistent basis, augmented with diffuse functions[53]. The aug-cc-pVQZ basis set for Hg was taken from Peterson and Puzzarini[54]. The molecular geometries of the XHgY molecules and the $XHgY.NO_3^-$ clusters (X,Y = OH, Cl, Br, I) were first optimized and their respective vibrational frequencies calculated. The geometries, rotational constants, vibrational frequencies and heats of formation (at 0 K) of the XHgY molecules and the $XHgY.NO_3^-$ clusters are listed in Table S3. The geometries of the cluster ions are illustrated in Fig. S9.

Photochemical and kinetics model details

Simulations in a (photo)chemical box model with the latest mercury chemical scheme[3,12,13,55] (Table S4). The model allows all the $Hg^{I,II}$ species to vary freely throughout the simulation, with their coupled continuity equations (ordinary differential equations) solved by using a Rosenbrock integrator. The simultaneous rate equations are converted into the differential equations using the KPP 2.2.3 kinetic preprocessor[56]. The photolysis rates were calculated using the absorption cross-sections, quantum yields and the actinic flux vertical profile, computed using the Tropospheric Ultraviolet and Visible (TUV) radiation model[57]. The actinic fluxes during May at 79° N, 0° E, were used as representative of springtime condition in polar regions. The model is constrained with 1.5 ng m^{-3} of Hg^0, 17 ppbv ozone, 90 ppbv CO, 1.95 ppmv CH_4, 8 pptv NO_2 and 45 pptv DMS. Two scenarios for high bromine (BrO peaking at 20 pptv) and low bromine (BrO peaking at 1 pptv) were run to represent bromine explosion and normal air mass events.

Data availability

The CI-APi-TOF and APi-TOF data generated in this study have been deposited in the Zenodo database: https://doi.org/10.5281/zenodo.15332305[58]. The data used in Fig. 3 are available from the Environment and Climate Change Canada: https://www.canada.ca/en/environment-climate-change/services/air-pollution/monitoring-networks-data/canadian-air-precipitation.html) and the European Monitoring and Evaluation Programme (EMEP): https://ebas-data.nilu.no.

References

1. Ariya, P. A. et al. Mercury physicochemical and biogeochemical transformation in the atmosphere and at atmospheric interfaces: a review and future directions. *Chem. Rev.* **115**, 3760–3802 (2015).
2. Horowitz, H. M. et al. A new mechanism for atmospheric mercury redox chemistry: implications for the global mercury budget. *Atmos. Chem. Phys.* **17**, 6353–6371 (2017).
3. Shah, V. et al. Improved mechanistic model of the atmospheric redox chemistry of mercury. *Environ. Sci. Technol.* **55**, 14445–14456 (2021).
4. Castro, P. J., Kellö, V., Cernušák, I. & Dibble, T. S. Together, not separately, OH and O3 Oxidize Hg(0) to Hg(II) in the atmosphere. *J. Phys. Chem. A* **126**, 8266–8279 (2022).
5. Sonke, J. E. et al. Global change effects on biogeochemical mercury cycling. *Ambio* **52**, 853–876 (2023).
6. Zhou, J., Obrist, D., Dastoor, A., Jiskra, M. & Ryjkov, A. Vegetation uptake of mercury and impacts on global cycling. *Nat. Rev. Earth Environ.* **2**, 269–284 (2021).
7. Bowman, K. L., Lamborg, C. H. & Agather, A. M. A global perspective on mercury cycling in the ocean. *Sci. Total Environ.* **710**, 136166 (2020).
8. Wang, S. et al. Direct detection of atmospheric atomic bromine leading to mercury and ozone depletion. *Proc. Natl. Acad. Sci. USA* **116**, 14479–14484 (2019).
9. Angot, H. et al. Chemical cycling and deposition of atmospheric mercury in polar regions: review of recent measurements and comparison with models. *Atmos. Chem. Phys.* **16**, 10735–10763 (2016).
10. Dastoor, A. et al. Arctic mercury cycling. *Nat. Rev. Earth Environ.* **3**, 270–286 (2022).
11. AMAP Assessment 2021: Mercury in the Arctic | AMAP. https://www.amap.no/documents/doc/amap-assessment-2021-mercury-in-the-arctic/3581.
12. Saiz-Lopez, A. et al. Photochemistry of oxidized Hg(I) and Hg(II) species suggests missing mercury oxidation in the troposphere. *Proc. Natl. Acad. Sci. USA* **117**, 30949–30956 (2020).
13. Saiz-Lopez, A. et al. The chemistry of mercury in the stratosphere. *Geophys. Res. Lett.* **49**, e2022GL097953 (2022).
14. Gustin, M. S. et al. Measurement of atmospheric mercury: current limitations and suggestions for paths forward. *Environ. Sci. Technol.* **58**, 12853–12864 (2024).

15. Gómez Martín, J. C. et al. The reaction between HgBr and O 3: kinetic study and atmospheric implications. *Phys. Chem. Chem. Phys.* **24**, 12419–12432 (2022).
16. Huang, J. & Gustin, M. S. Uncertainties of gaseous oxidized mercury measurements using KCl-coated denuders, cation-exchange membranes, and nylon membranes: humidity influences. *Environ. Sci. Technol.* **49**, 6102–6108 (2015).
17. Landis, M. S., Stevens, R. K., Schaedlich, F. & Prestbo, E. M. Development and characterization of an annular denuder methodology for the measurement of divalent inorganic reactive gaseous mercury in ambient air. *Environ. Sci. Technol.* **36**, 3000–3009 (2002).
18. Cheng, I. & Zhang, L. Uncertainty assessment of gaseous oxidized mercury measurements collected by atmospheric mercury network. *Environ. Sci. Technol.* **51**, 855–862 (2017).
19. Bu, X. et al. Comparison of reactive gaseous mercury collection by different sampling methods in a laboratory test and field monitoring. *Environ. Sci. Technol. Lett.* **5**, 600–607 (2018).
20. McClure, C. D., Jaffe, D. A. & Edgerton, E. S. Evaluation of the KCl denuder method for gaseous oxidized mercury using HgBr2 at an in-service AMNet Site. *Environ. Sci. Technol.* **48**, 11437–11444 (2014).
21. Luippold, A., Gustin, M. S., Dunham-Cheatham, S. M. & Zhang, L. Improvement of quantification and identification of atmospheric reactive mercury. *Atmos. Environ.* **224**, 117307 (2020).
22. Junninen, H. et al. A high-resolution mass spectrometer to measure atmospheric ion composition. *Atmos. Meas. Tech.* **3**, 1039–1053 (2010).
23. Jokinen, T. et al. Atmospheric sulphuric acid and neutral cluster measurements using CI-APi-TOF. *Atmos. Chem. Phys.* **12**, 4117–4125 (2012).
24. Jokinen, T. et al. Ion-induced sulfuric acid–ammonia nucleation drives particle formation in coastal Antarctica. *Sci. Adv.* **4**, eaat9744 (2018).
25. Shupe, M. D. et al. Overview of the MOSAiC expedition: atmosphere. *Elem. Sci. Anthr.* **10**, 00060 (2022).
26. Benavent, N. et al. Substantial contribution of iodine to Arctic ozone destruction. *Nat. Geosci.* **15**, 770–773 (2022).
27. Bianchi, F. et al. The role of highly oxygenated molecules (HOMs) in determining the composition of ambient ions in the boreal forest. *Atmos. Chem. Phys.* **17**, 13819–13831 (2017).
28. Kürten, A., Rondo, L., Ehrhart, S. & Curtius, J. Calibration of a chemical ionization mass spectrometer for the measurement of gaseous sulfuric acid. *J. Phys. Chem. A* **116**, 6375–6386 (2012).
29. Sipilä, M. et al. Molecular-scale evidence of aerosol particle formation via sequential addition of HIO3. *Nature* **537**, 532–534 (2016).
30. Tham, Y. J. et al. Widespread detection of chlorine oxyacids in the Arctic atmosphere. *Nat. Commun.* **14**, 1769 (2023).
31. Ehn, M. et al. A large source of low-volatility secondary organic aerosol. *Nature* **506**, 476–479 (2014).
32. Boyer, M. et al. The annual cycle and sources of relevant aerosol precursor vapors in the central Arctic during the MOSAiC expedition. *Atmos. Chem. Phys.* **24**, 12595–12621 (2024).
33. Yue, F. et al. The Marginal Ice Zone as a dominant source region of atmospheric mercury during central Arctic summertime. *Nat. Commun.* **14**, 4887 (2023).
34. Angot, H. et al. Gaseous elemental mercury concentrations measured in the University of Colorado container during the 2019-2020 MOSAiC (Multidisciplinary drifting Observatory for the Study of Arctic Climate) expedition. https://doi.org/10.18739/A2C824G3G (2022) doi:10.18739/A2C824G3G.
35. Burd, J. A., Peterson, P. K., Nghiem, S. V., Perovich, D. K. & Simpson, W. R. Snowmelt onset hinders bromine monoxide heterogeneous recycling in the Arctic. *J. Geophys. Res. Atmos.* **122**, 8297–8309 (2017).
36. Ahmed, S. et al. Modelling the coupled mercury-halogen-ozone cycle in the central Arctic during spring. *Elem. Sci. Anthr.* **11**, 00129 (2023).
37. Steffen, A. et al. A synthesis of atmospheric mercury depletion event chemistry in the atmosphere and snow. *Atmos. Chem. Phys.* **8**, 1445–1482 (2008).
38. Dommergue, A. et al. Overview of mercury measurements in the Antarctic troposphere. *Atmos. Chem. Phys.* **10**, 3309–3319 (2010).
39. MacSween, K. et al. Updated trends for atmospheric mercury in the Arctic: 1995–2018. *Sci. Total Environ.* **837**, 155802 (2022).
40. Osterwalder, S. et al. Fate of springtime atmospheric reactive mercury: concentrations and deposition at Zeppelin, Svalbard. *ACS Earth Space Chem.* **5**, 3234–3246 (2021).
41. Osterwalder, S. et al. Correction to Fate of Springtime Atmospheric Reactive Mercury: Concentrations and Deposition at Zeppelin, Svalbard. *ACS Earth Space Chem.* **6**, 249–249 (2022).
42. Saiz-Lopez, A. et al. Role of the stratosphere in the global mercury cycle. *Sci. Adv.* **11**, eads1459 (2025).
43. Mao, N. & Khalizov, A. Exchange reactions alter molecular speciation of gaseous oxidized mercury. *ACS Earth Space Chem.* **5**, 1842–1853 (2021).
44. Saiz-Lopez, A. et al. Gas-Phase Photolysis of Hg(I) Radical Species: A New Atmospheric Mercury Reduction Process. *J. Am. Chem. Soc.* **141**, 8698–8702 (2019).
45. Saiz-Lopez, A. et al. Photoreduction of gaseous oxidized mercury changes global atmospheric mercury speciation, transport and deposition. *Nat. Commun.* **9**, 4796 (2018).
46. Lee, C. F. et al. Elevated tropospheric iodine over the central continental United States: Is iodine a major oxidant of atmospheric mercury?. *Geophys. Res. Lett.* **51**, e2024GL109247 (2024).
47. Beck, L. J. et al. Differing mechanisms of new particle formation at two Arctic Sites. *Geophys. Res. Lett.* **48**, e2020GL091334 (2021).
48. Baccarini, A. et al. Low-volatility vapors and new particle formation over the southern ocean during the antarctic circumnavigation expedition. *J. Geophys. Res. Atmos.* **126**, e2021JD035126 (2021).
49. Curtius, J. et al. Isoprene nitrates drive new particle formation in Amazon's upper troposphere. *Nature* **636**, 124–130 (2024).
50. Kyrö, E.-M. et al. Antarctic new particle formation from continental biogenic precursors. *Atmos. Chem. Phys.* **13**, 3527–3546 (2013).
51. Beck, I. et al. Automated identification of local contamination in remote atmospheric composition time series. *Atmos. Meas. Tech.* **15**, 4195–4224 (2022).
52. Frisch, M. J. et al. Gaussian 16 Rev. C.01. (Wallingford CT, 2016).
53. Woon, D. E. & Dunning, T. H. Gaussian basis sets for use in correlated molecular calculations. III. The atoms aluminum through argon. *J. Chem. Phys.* **98**, 1358–1371 (1993).
54. Peterson, K. A. & Puzzarini, C. Systematically convergent basis sets for transition metals. II. Pseudopotential-based correlation consistent basis sets for the group 11 (Cu, Ag, Au) and 12 (Zn, Cd, Hg) elements. *Theor. Chem. Acc.* **114**, 283–296 (2005).
55. Francés-Monerris, A. et al. Photodissociation mechanisms of major mercury(II) species in the atmospheric chemical cycle of mercury. *Angew. Chem. Int. Ed.* **59**, 7605–7610 (2020).
56. Damian, V., Sandu, A., Damian, M., Potra, F. & Carmichael, G. R. The kinetic preprocessor KPP-a software environment for solving chemical kinetics. *Comput. Chem. Eng.* **26**, 1567–1579 (2002).
57. Madronich, S. & Flocke, S. The Role of Solar Radiation in Atmospheric Chemistry. in *Environmental Photochemistry* (ed. Boule, P.) 1–26 (Springer, Berlin, Heidelberg, 1999). https://doi.org/10.1007/978-3-540-69044-3_1.
58. Jokinen, T. Direct observations of atmospheric oxidized mercury in polar areas. *Zenodo* https://doi.org/10.5281/zenodo.15332305 (2025).

Acknowledgements
We thank Shrutika P. Wagn for data analysis support. Data reported in this manuscript were produced as part of the international Multidisciplinary drifting Observatory for the Study of Arctic Climate (MOSAiC) expedition with the tag MOSAiC20192020, with activities supported by Polarstern expedition AWI_PS122_00. We thank everyone at the University of Helsinki, Paul Scherrer Institute and EPFL who contributed to the success of this expedition and for all technical and logistical support. Support of University of Helsinki, Faculty of Science via ACTRIS-HY is gratefully acknowledged. This project has received funding from the European Union's Horizon 2020 research and innovation programme under grant agreement No. 856612 and the Cyprus Government (T.J.). Funded by the European Union ERC-2022-STGERC-BAE-Project: 101076311 (T.J.). Views and opinions expressed are however those of the author(s) only and do not necessarily reflect those of the European Union or the European Research Council Executive Agency. Neither the European Union nor the granting authority can be held responsible for them. This work has received support from the European Union's Horizon 2020 research and innovation programme under grant agreement No 101003826 (Climate Relevant interactions and feedbacks: the key role of sea ice and Snow in the polar and global climate system, CRiceS, M.K., T.P.) and under agreement 101056783 (Non-CO2 Forcers And Their Climate, Weather, Air Quality And Health Impacts, FOCI). Part of this project (Aboa campaign) was funded by ERC-StG (GASPARCON, 714621, M.S.). We acknowledge funding from the Spanish Ministry of Science and Innovation (MCIN/AEI/ 10.13039/501100011033) through grants Severo Ochoa CEX2021-001131-S, PID2021-123370OB-I00 and CNS2020-135828, and the European Union NextGenerationEU/PRTR (JCGM). We acknowledge funding from Horizon Europe Marie Skłodowska-Curie grant agreement 101103544 (A.F.). The Indian Institute of Tropical Meteorology is funded by the Ministry of Earth Sciences, Government of India (A.S.M.). Research council of Finland (Antarctic Climate Forcing Aerosol, ACFA, 335844, T.P.). The ACCC Flagship is funded by the Research Council of Finland with the following grant numbers; 337549, 357902, 359340 (M.K.). European Research Council (ERC) project ATM-GTP Contract No. 742206 (M.K.). The Swiss National Science Foundation (grant nos. 200021_188478, J.S.). The Swiss polar Institute (grant no. DIRCR-2018-004, JS). We acknowledge funding from the US Department of Energy grants DE-SC0022046 (J.S.). JS holds the Ingvar Kamprad Chair for Extreme Environments Research sponsored by Ferring Pharmaceuticals. We acknowledge support from the Scientific Network PolarCSIC funded by the Consejo Superior de Investigaciones Científicas (CSIC), Spain (A.S.L.).

Author contributions
Conceptualization: A.S.L., J.C.G.M., T.J., A.U.A. Methodology: T.J., L.Q., T.L., I.B., J.S., M.S., M.K., T.P., H.J. Investigation: J.C.G.M., A.F., A.S.L., T.J., A.S.M., J.M.C.P., A.U.A., J.D., C.C. Modelling: A.S.M. Visualization: T.J., A.S.M., J.C.G.M., A.F. Funding acquisition: T.J., M.K., T.P., J.S., M.S. Project administration: A.S.L., T.J. Supervision: A.S.L., T.J. Writing—original draft: T.J., J.C.G.M., A.F., A.S.M., A.S.L. Writing—review and editing: all authors

Competing interests
The authors declare no competing interests.

Additional information
Supplementary information The online version contains supplementary material available at https://doi.org/10.1038/s41467-026-71146-z.

Correspondence and requests for materials should be addressed to Tuija Jokinen or Alfonso Saiz-Lopez.

Peer review information *Nature Communications* thanks Dan Jaffe and the other, anonymous, reviewer(s) for their contribution to the peer review of this work. A peer review file is available.